PAPER • **OPEN ACCESS**

ML-EM based dual tracer PET image reconstruction with inclusion of prompt gamma attenuation

To cite this article: Elisabeth Pfaehler *et al* 2025 *Phys. Med. Biol.* **70** 015009

IOP Publishing Phys. Med. Biol. 70 (2025) 015009 https://doi.org/10.1088/1361-6560/ad9660

Physics in Medicine & Biology

IPEM Institute of Physics and Engineering in Medicine

OPEN ACCESS

RECEIVED
22 August 2024

REVISED
14 November 2024

ACCEPTED FOR PUBLICATION
22 November 2024

PUBLISHED
24 December 2024

PAPER

ML-EM based dual tracer PET image reconstruction with inclusion of prompt gamma attenuation

Elisabeth Pfaehler[1,*], **Debora Niekämper**[1], **Jürgen Scheins**[1], **N Jon Shah**[1,2,3,4] and **Christoph W Lerche**[1]

[1] Institute for Neuroscience and Medicine 4, INM-4, Forschungszentrum Jülich GmbH, Jülich, Germany
[2] Institute of Neuroscience and Medicine 11, INM-11, JARA, Forschungszentrum Jülich, Jülich, Germany
[3] JARA—BRAIN—Translational Medicine, Aachen, Germany
[4] Department of Neurology, RWTH Aachen University, Aachen, Germany
[*] Author to whom any correspondence should be addressed.

E-mail: e.pfaehler@fz-juelich.de

Keywords: positron emission tomography, dual tracer PET, maximum-likelihood expectation maximization

Supplementary material for this article is available online

Abstract

Objective. Conventionally, if two metabolic processes are of interest for image analysis, two separate, sequential positron emission tomography (PET) scans are performed. However, sequential PET scans cannot simultaneously display the metabolic targets. The concurrent study of two simultaneous PET scans could provide new insights into the causes of diseases. *Approach.* In this work, we propose a reconstruction algorithm for the simultaneous injection of a β^+-emitter emitting only annihilation photons and a β^+-γ-emitter emitting annihilation photons and an additional prompt γ-photon. As in previous works, the γ-photon is used to identify events originating from the β^+-γ-emitter. However, due to e.g. attenuation and down-scatter, the γ-photon is often not detected and not all events can correctly be associated with the β^+-γ-emitter as they are detected as double coincidences. In contrast to previous works, we estimate this number of double coincidences with origin in the β^+-γ, emitter including the attenuation of the prompt γ, and incorporate this estimation in the forward-projection of the maximum likelihood expectation maximization algorithm. For evaluation, we simulate different scenarios with varying objects and attenuation maps. The nuclide ^{18}F serves as β^+-emitter, while ^{44}Sc functions as β^+-γ emitter. The performance of the algorithm is assessed by calculating the residual error of the β^+-γ-emitter in the reconstructed β^+-emitter image. Additionally, the intensity values in the simulated cylinders of the ground truth (GT) and the reconstructed images are compared. *Main results.* The remaining activity in the β^+-emitter image varied from 0.4% to 3.7%. The absolute percentage difference between GT and reconstructed intensity for the pure β^+ emitter images was found to be between 3.0% and 7.4% for all cases. The absolute percentage difference between the GT and the reconstructed intensity for the β^+-γ emitter images ranged from 8.7% to 10.4% for all simulated cases. *Significance.* These results demonstrate that our approach can reconstruct two separate images with a good quantitation accuracy.

1. Introduction

Positron emission tomography (PET) is an imaging method routinely used in oncology, neurology, cardiology, and psychiatry (Chételat *et al* 2020, Salaün *et al* 2020, Meikle *et al* 2021). Before PET image acquisition, a radio-active compound (radiotracer) is administered to the patient. This radiotracer is distributed in the body and accumulates in tissue through trapping or specific binding. Depending on the radiotracer, different metabolic processes can be quantified in the corresponding PET image. Conventionally, the patient is only injected with one tracer, and therefore only one functional or metabolic process can be visualized and quantified at a time. However, the simultaneous visualization and quantization of two

metabolic processes could provide new insights into diseases and a better understanding of the interplay between biological receptor systems, e.g. excitatory and inhibitory neurotransmitters and neuroreceptors. However, to allow the reconstruction of two independent images from a single acquisition with two simultaneously injected radiotracers, the detected coincidences need to be separated. As both annihilation photons yield an energy of 511 keV independent of the radiotracer, separation is challenging.

The use of staggered injections is one proposed technique to separate the signal of two radio-tracers (Black *et al* 2009, Gao *et al* 2009, Kadrmas *et al* 2013). In this case, the contribution of each tracer to the detected coincidences is estimated using kinetic constraints obtained from the corresponding dynamic PET images. Although this technique can provide good results, the scan time is necessarily longer than the typical scan time for a single tracer application (approx. 60 min) (Rust *et al* 2006). Furthermore, the separation of the tracers requires optimization and adjustment for each specific tracer combination (Kadrmas *et al* 2013).

Another group used convolutional neural networks (CNNs) for dual tracer PET image reconstruction (Zeng *et al* 2023). Using animal or simulated data, a CNN is trained to separate the images into individual contributions from the tracers. The results of these studies demonstrated that neural networks can be used for dual tracer PET reconstruction. However, they only yield good results for data very similar to the training data. As demonstrated in Fang *et al* (2024), a CNN trained to reconstruct brain images, can only be applied to brain images and not to e.g. reconstruct lung PET scans.

Other approaches have sought to combine one pure positron emitter (β^+-emitter) emitting two annihilation γ-photons and a non-pure positron emitter (β^+-γ-emitter) emitting an additional prompt high-energy γ-photon (Andreyev and Celler 2011, Pratt *et al* 2023). As the positronium lifetime in water lies approximately between 2 and 9 ns (Steinberger *et al* 2024), the two annihilation photons and the prompt γ-photon lie in the same time window. Therefore, by detecting the prompt γ-photon and two annihilation photons in the same time window, the list mode data can be separated into double and triple coincidences for many nuclides. The energy of the prompt γ-photon is tracer-dependent (see table 1). However, not all coincidences with origin in the β^+-γ-emitter are detected as triple coincidences due to the limited detection efficiency of the PET scanner. Moreover, similarly to annihilation photons, the prompt γ-photons are also subject to attenuation dominated by Compton scattering. Consequently, a considerable number of prompt γ-photons may not be detected because they escape without hitting a scintillation detector after scattering. Additionally, the γ-photon can be down-scattered, i.e. the energy of the secondary γ-photon after scattering can be too low for the energy acceptance window. Therefore, events originating from the β^+-γ-emitter can also be detected as a pure annihilation γ-photon pair (without prompt γ detection) giving rise to triple coincidences that are incorrectly detected as double coincidences. These events are therefore falsely associated with the pure β^+-emitter. The amount of incorrectly detected double coincidences depends on the branching ratio of the isotope, the position of the source in the field-of-view (FOV), the PET scanner geometry, and the scanned object, which causes attenuation and down-scatter.

As the fraction of double coincidences with origin in the β^+-γ-emitter needs to be accurately estimated to provide proper separation of both tracers, several groups have used a scan of a phantom filled with an aqueous solution of the β^+-γ-emitter (Fukuchi *et al* 2021, Pratt *et al* 2023) to estimate the fraction of incorrectly identified double coincidences. Using this phantom scan, a ratio matrix is determined to indicate the detected ratio between triple and double events originating from the β^+-γ-emitter for each position across the FOV. To reconstruct two separate images, one image is reconstructed using all double coincidences, and one image is reconstructed using all triple coincidences. Hereby, two photons with an energy range between 350 keV and 650 keV detected within the coincidence time window are considered as double coincidences. Similarly, when an additional high-energy γ-photon ($>$650 keV) is detected in the same coincidence time window, the event is considered as triple coincidence. Next, the estimated ratio matrix is used to determine the contribution of the β^+-γ-emitter to the double-coincidence image. This contribution is then consecutively subtracted from the double-coincidence image and added to the triple-coincidence image (Andreyev *et al* 2014, Fukuchi *et al* 2021, Pratt *et al* 2023). In this way, two separate images are reconstructed. However, the scan of a cylindrical phantom only gives a rough estimation of the number of double events originating in the β^+-γ-emitter as it does not include the correct attenuation and down-scatter of the scanned object. Additionally, the subtraction of a part of the double-coincidence image can lead to non-physical negative image values.

In a previous work, a maximum likelihood expectation maximization algorithm (ML-EM) for the reconstruction of simulated dual tracer PET images was presented assuming a constant triple detection efficiency across the FOV (Sitek *et al* 2011). While this approach can be expected to lead to an acceptable quantitation accuracy for dual tracer imaging of small objects like mice and rats, neglecting attenuation and down-scattering may lead to considerable quantitation errors when scanning large animals or humans. As shown in figure 1(upper left), the remaining energy after Compton scattering of high-energy γ-photons depends heavily on the scatter angle, of which the probability distribution is governed by the Klein–Nishina

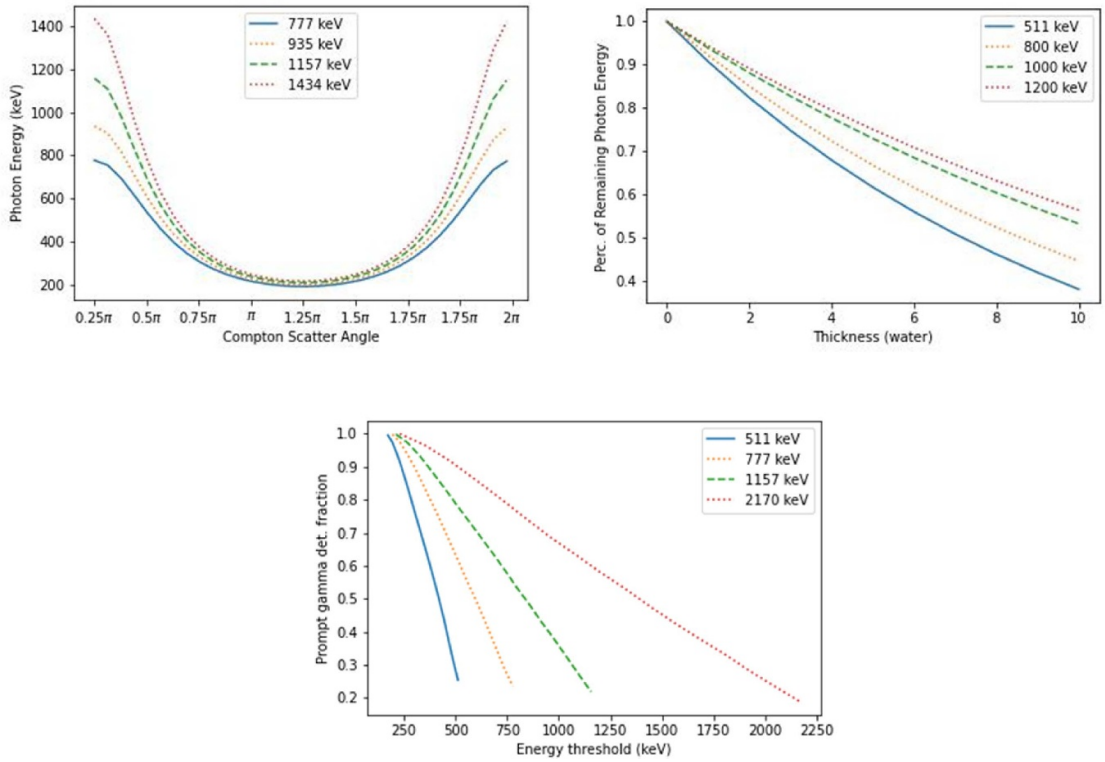

Figure 1. Upper Left: remaining energy after Compton scattering for high energy γ-photons depending on the scatter angle. Upper Right: non-attenuated fraction of γ-photons for γ-photons with different energies after passing through up to 10 cm of water according to the Beer–Lambert attenuation law. Lower image: fraction of detectable down-scattered γ-photons vs. energy thresholds for different γ-photon energies.

Table 1. Table of radio-nuclides especially suitable for dual tracer PET imaging using the prompt γ-photons (^{22}Na only in phantoms) (Conti and Eriksson 2016).

Isotope	Half-life	Positron emission prob.	Prompt gamma prob.	Prompt γ energy
^{22}Na	2.7 years	90%	100%	1274 keV
^{44}Sc	3.97 h	94.27%	100%	1157 keV
^{82}Rb	1.3 min	94.9%	15.1%	777 keV
^{38}K	7.61 min	99%	99%	2170 keV
^{52}Mn	5.59 days	29.4%	90%	744 keV
			94.5%	935.5 keV
			100%	1434 keV
^{60}Cu	23.4 min	92.5%	21%	826 keV
			88%	1332 keV
			46%	1792 keV

cross-section. In figure 1, upper right, the non-attenuated fraction of prompt γ-photons with different energies is given for traversing hypothetical objects consisting of pure water and for sizes ranging from 0 cm to 10 cm. The lower part of figure 1 shows the impact of down-scatter on the fraction of γ-photons with different energies undergoing exactly one Compton interaction (with an unbound electron) and detected above a chosen energy threshold. Overall, after attenuation in material, a large number of high-energy γ-photons are not accepted in the energy window due to the high energy loss.

Throughout this work, we focus on β^+-γ-emitters emitting a single prompt γ-photon with an energy high enough to ensure sufficient separation of the full absorption peaks in the corresponding energy spectra. Various radioisotopes fulfill this condition (see table 1).

Besides emitting a high-energy γ-photon, the β^+-γ-emitter should also allow for the radio-synthesis of isotopes suitable for providing complementary and relevant biological information. From the radioisotopes listed in table 1, it can be seen that ^{22}Na is not suitable for use in a clinical scenario due to it is long half-life. However, it is often used as a test source for PET imaging because of the good energy separability of the prompt γ. In contrast, ^{44}Sc is one promising β^+-γ-emitter that can be used in the clinic. Previous studies

have demonstrated the suitability of ^{44}Sc-PSMA to target the prostate-specific membrane antigen (Umbricht *et al* 2017) suggesting it could be an alternative to ^{68}Ga. Additionally, in earlier work, ^{44}Sc labeled arginine-glycine-aspartic acid was used to highlight the overexpression of integrin $\alpha_v\beta_3$, an indicator of tumor aggressiveness and metastasis in several cancer types (Hernandez *et al* 2014). The radionuclides ^{82}Rb and ^{38}K are used to display myocardial blood flow (Myers 1973) and could e.g. be used in combination with ^{18}F-Fluorodeoxyglucose (FDG) which is used to detect e.g. cardiac infections (Erba *et al* 2013). Other studies have demonstrated the potential of ^{52}Mn for its use in neuronal or tumor imaging (Topping *et al* 2013, Graves *et al* 2015). ^{60}Cu is used for assessing tumor hypoxia (Dehdashti *et al* 2003) and could also be used in combination with e.g. ^{18}F-FDG displaying tumor glucose consumption.

In this work, we propose a new approach which provides an accurate estimation of the number of events originating in the β^+-γ-emitter that are detected as double coincidences. Hereby, the number of double coincidences associated with the β^+-γ-emitter are estimated by considering the position in the FOV and the actual object attenuation. This number is then incorporated in the forward projection of the ML-EM algorithm such that all necessary corrections, such as random, scatter, and attenuation correction can be performed without violating the positivity constraint of the ML-EM algorithm. The two separate quantitative PET images are then simultaneously reconstructed. In this work, we combine the tracers ^{18}F and ^{44}Sc. However, the proposed algorithm is not limited to the separation of these tracers. For illustration purposes, we used a tracer with a high-energy prompt γ-photon. However, the reconstruction procedure can be extended to other isotopes.

While consideration is given to the attenuation of the prompt γ-photon and down-scatter due to the object, for the sake of simplicity, scatter correction is not applied. This will be implemented in a future version of the algorithm. Furthermore, random and scatter correction of the annihilation photon pair is not considered. However, the proposed algorithm can be appropriately extended without violating the positivity constraint of the ML-EM algorithm. The positron range, wrongly detected double coincidences due to the down-scatter of the high-energy photon, and positronium lifetime have not been considered throughout this work as these aspects should have little impact on the results. In our simulations, around 3% of all detected coincidences were incorrectly detected as double coincidences (i.e. one scattered prompt γ-photon and one annihilation photon). From these 3% only 1.5% resulted in LORs crossing the FOV. The proposed algorithm was evaluated using simulated images.

2. Materials and methods

2.1. Reconstruction overview

The proposed dual tracer reconstruction workflow includes the following steps (see figure 2):

- Estimation by simulations: estimate geometry and nuclide dependent detection ratio η_j of triple and double events with origin in β^+-γ-emitter for each voxel *j*: This ratio is system dependent and can be calculated and stored once for each scanner and isotope.
- Update the ratio η_j by the object attenuation to $\tilde{\eta}_j$ for each voxel *j*: this ratio is object dependent and needs to be calculated for each patient and each phantom separately.
- Separate list mode data in double and triple coincidences using the detected prompt γ-photons.
- Reconstruct the β^+-γ-emitter image Λ^{γ} including attenuation correction using the position and attenuation dependent triple-to-double detection ratio $\tilde{\eta}_j$.
- Reconstruct the pure β^+-emitter image Λ^{β^+} including all double coincidences, containing those doubles from pure β^+ of the β^+-γ emitter and incorporating the corrected triple coincidence image in the forward projection of the algorithm according to the ordinary Poisson iterative reconstruction approach (Michel *et al* 1998).

For simplicity and to maintain generality, the system matrix is calculated using the Siddon algorithm. The attenuation factors are calculated via ray tracing considering single representative lines of responses. In the simulations, a detected photon pair where both photon energies are in the energy range of the established energy window (400–600 keV) is considered a double coincidence. All other double coincidences (e.g. the detection of one 511 keV photon and one high-energy γ) are ignored.

2.2. Estimation of triple-to-double ratio

An accurate estimation of the number of double events originating in the decays of the β^+-γ-emitter is essential for the accurate separation of both tracers. This estimation is performed using the known number of detected triple coincidences and an estimated ratio of triple and expected double events originating from the β^+-γ-emitter. The calculation of this ratio consists of two parts:

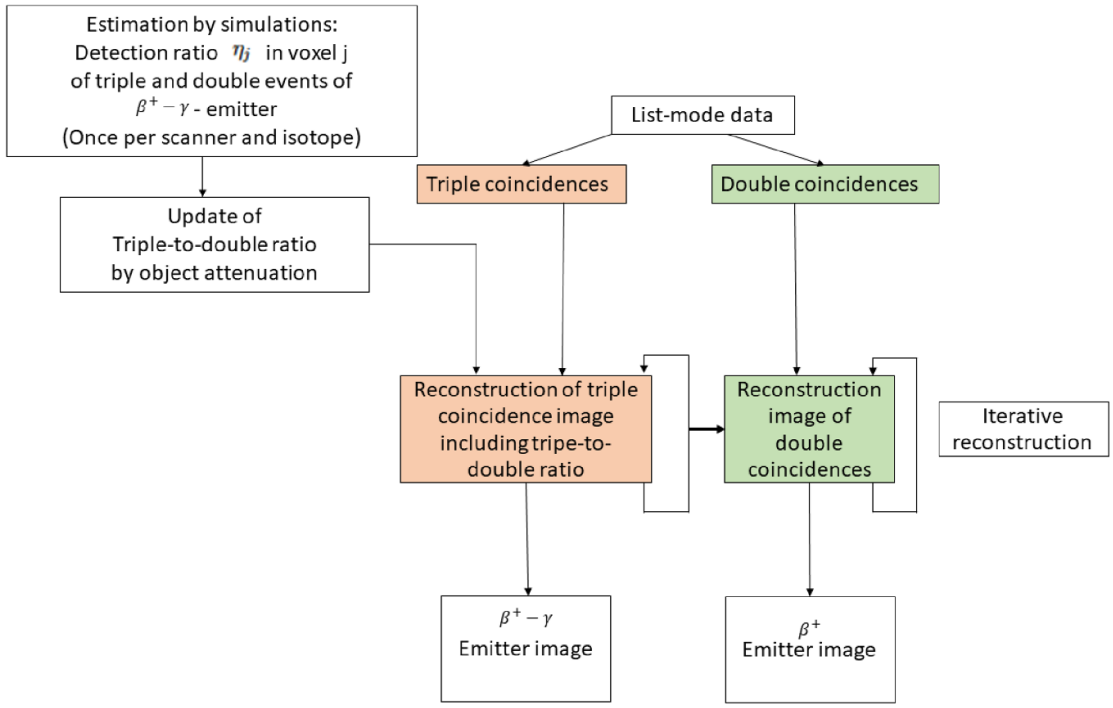

Figure 2. Overview of the steps included in the reconstruction process.

2.2.1. Ratio dependent on the detection efficiency in the FOV location and branching ratios

In this step, the triple-to-double ratio of events originating from the β^+-γ-emitter in different FOV locations is estimated. This estimation is performed using Monte Carlo (MC) simulations assuming no object attenuation. The ratio depends on the PET ring configuration, the location of the source in the scanner's FOV, and the branching ratios of β^+-γ dependent decays of the current isotope. The effect of the branching ratios on the triple-to-double ratio is included in the MC simulation but can also be implemented as a position-independent factor for the triple detection efficiency. Hereby, a point source mimicking a realistic β^+-γ-emitter is placed in different locations that differ by 1 cm in each direction (x, y, or z). For each location and radiotracer, a separate MC simulation is performed. For each simulation, the ratio of detected double and triple events is recorded. Note that this triple-to-double ratio η_j can also be regarded as the general detection efficiency of triple coincidences at the current location. This detection efficiency corresponds to the detection efficiency of the high-energy γ-photon under the condition that two annihilation photons were detected (see supplemental material, section 1). Thus, η_j can be written as $\eta_j = p_j^{\gamma} \sum_i c_{i,j}$, where p_j^{γ} is the probability to detect a prompt γ-photon and $c_{i,j}$ is the detection probability of an annihilation photon pair in the detector pixel pair i (i.e. the LOR) if the annihilation occurred in image voxel j (i.e. the system matrix element). The ratio is then stored at the corresponding voxel position j in a matrix with the desired image size. The ratio between the simulated locations is interpolated using tri-linear interpolation. Our experiments showed that the triple-to-double ratio is similar for locations close together in the FOV (see supplemental material, section 2). The scanner-dependent triple-to-double ratio can also be acquired by placing a point source on different positions in the real scanner FOV and recording the exact position and the triple-to-double ratio. Similar to simulations, the triple-to-double ratio can be interpolated between points and can be stored at the corresponding positions in a matrix. As this matrix is only dependent on the scanner geometry, this calibration can be performed once for each scanner and isotope. The ratio map, which depends on the FOV location and branching ratio varies with the isotope and scanner used. Therefore, it must be individually calculated for each scanner and nuclide.

2.2.2. Ratio update according to attenuation of prompt γ-photons

As illustrated in figure 1, a considerable fraction of high-energy photons lose a significant amount of their energy during scattering. Therefore, these photons are often not detected and the corresponding triple events are not identified as such. This implies that the object attenuation has an impact on the triple-to-double ratio of events from the β^+-γ-emitter, especially for large objects. Attenuation also affects the number of detected double coincidences. However, it affects the annihilation photons of β^+- and β^+-γ-emitter equally as they yield the same kinetic energy. Therefore, the attenuation of the double coincidences does not impact the

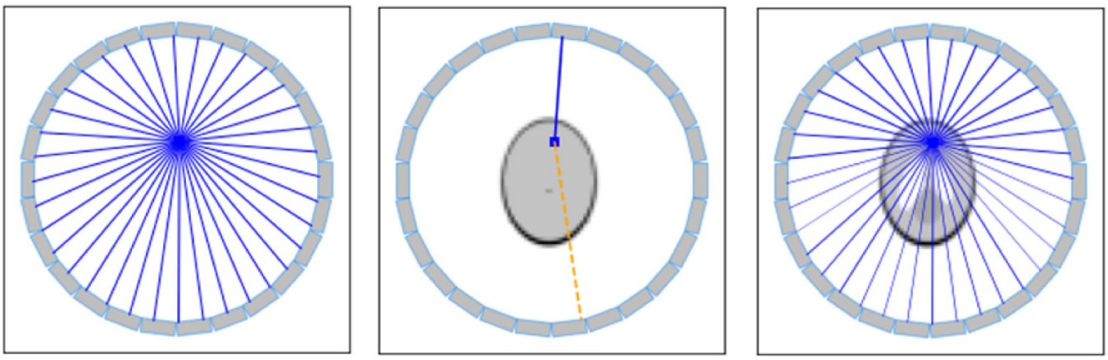

Figure 3. Left: ratio estimation based on FOV location including detection efficiency and branching ratios. MC simulations are performed without an object in the FOV. Middle: one high-energy photon is emitted in a voxel position and detected in a detector element (blue connected line). If the corresponding attenuation factor is used to update the triple-to-double ratio, the ratio is underestimated as there are other detector elements where the attenuation would be much higher (orange dashed line). Right: illustration of the calculation of the mean attenuation factor for one voxel: for each voxel the attenuation between the voxel position and each detector element is calculated. The mean attenuation over all possible paths is then calculated and used to update the FOV-dependent triple-to-double ratio.

triple-to-double ratio as this factor appears in the nominator and denominator of the ratio. The joined emission and detection ratio η_j derived from point source MC simulations is therefore multiplied with the attenuation factor corresponding to the prompt γ-photon. Hereby, the attenuation coefficient corresponding to the energy of the prompt γ-photon is used. In case of ^{44}Sc, the attenuation coefficient is 0.069 for water and 0.127 for bone.

For the computation of the effect of attenuation, considering the attenuation factor corresponding to the path between a voxel and the individual detector pixel where the γ-photon was detected would result in approximation errors as illustrated in figure 3(middle). The detection efficiency of a triple coincidence is small. Therefore, the detected triple events are only a small representation of all possible triple events. As a consequence, the attenuation factors corresponding to the detected γ-photons are also only a random representation of all possible attenuation factors. If the triple-to-double ratio would be updated by the attenuation factor corresponding to the detected triple events, the triple-to-double ratio could be over- or underestimated. I.e. if a detected γ-photon is crossing only a short part of the brain, the attenuation factor is high. On contrary, if the γ-photon crosses a large part of the brain, the attenuation factor is small. In both of these cases, it can happen that the triple-to-double ratio is over- or underestimated as only the detected coincidences are included. However, the attenuation factors of the detected triple coincidences are likely not exactly the same as for the detected double coincidences (which would have been detected as triple coincidences without attenuation). To avoid these over- or underestimations, we calculate the attenuation for each possible voxel-detector path (as illustrated in figure 3). The mean of all attenuation factors $\overline{\alpha_{j_\gamma}}$ is then used to update the triple-to-double ratio:

$$\widetilde{\eta_j} = \eta_j \cdot \overline{\alpha_{j_\gamma}}. \tag{1}$$

Using this updated ratio, the number of double coincidences originating from decays from the β^+-γ-emitter can be estimated and subsequently included in the reconstruction procedure.

2.3. Image reconstruction of the triple coincidence image including the triple-to-double ratio

The previously estimated triple-to-double ratio $\widetilde{\eta_j}$ includes the triple detection efficiency and the attenuation of the prompt γ-photon. By including the ratio in the reconstruction of the image corresponding to the detected triple coincidences, the expected number of double coincidences in voxel λ_j^γ originating from the decay of the β^+-γ emitter can be estimated from the detected triples:

$$\begin{aligned}\lambda_{j,n+1}^\gamma &= \frac{\lambda_{j,n}^\gamma}{\widetilde{\eta_j}\sum_i \alpha_i c_{i,j}} \sum_i \frac{\alpha_i \widetilde{\eta_j} c_{i,j} b_i^\gamma}{\alpha_i \sum_k c_{i,k}\widetilde{\eta_k}\lambda_{k,n}^\gamma} \\ &= \frac{\lambda_{j,m}^\gamma}{\sum_i \alpha_i c_{i,j}} \sum_i \frac{c_{i,j} b_i^\gamma}{\sum_k c_{i,k}\widetilde{\eta_k}\lambda_{k,n}^\gamma}\end{aligned} \tag{2}$$

Hereby, $\lambda_{j,n}^\gamma$ is the activity corresponding to the β^+-γ-emitter and present in voxel j at iteration n. The probability that an annihilation-γ pair emitted from the position of voxel j is detected in the detector pair

connecting the LOR i is denoted as $c_{i,j}$. The attenuation factor corresponding to the LOR i for double coincidences is shown by α_i. Detected triple events in the LOR i are given by b_i^γ. The iteration begins with a homogeneous image where all voxels are initialized $\lambda_{j,0}^\gamma = 1$.

2.4. Separate list mode data in double and triple coincidences

As previous groups have already reported on the separation of the list mode data in double and triple coincidences (Andreyev and Celler 2011, Fukuchi *et al* 2021, Pratt *et al* 2023), and this was also not the focus of our work, we did not develop a list mode separation using coincidence windows. We rather used the event ID that marks different decay events provided by the MC simulation to identify single events. Together with the corresponding number of detected coincidences, the list-mode data was separated into triple and double coincidences. Also, in this way, all random events were excluded from the analysis. Inter-crystal scattered events were suppressed (by energy filtering).

2.5. Reconstruction of the pure β^+-emitter image

All detected double coincidences are included for the reconstruction of the pure β^+-emitter image. The number of all detected double events is the sum of double events from the β^+-emitter decays and the double events from β^+-γ-emitter decays without prompt-γ detection:

$$b_i^D = b_i^{\beta^+} + b_i^{D-\gamma}. \tag{3}$$

Hereby, b_i^D refers to all detected double events along the LOR i, $b_i^{\beta^+}$ refers to the detected double coincidences from the pure β^+-emitter and $b_i^{D-\gamma}$ is the double coincidences detected from the β^+-γ emitter. Equation (3) only shows the information for all detected double coincidences and not the individual contributions. However, the number of detected double coincidences originating from the β^+-γ-emitter can be estimated using the triple-to-double ratio and the detected triple coincidences.

The expected value of measured double coincidences corresponding to the LOR i and the β^+-emitter is estimated as:

$$\widetilde{b_i^{\beta^+}} = \sum_k c_{ik} \cdot \lambda_k^{\beta^+}. \tag{4}$$

Equally, the expected values of the measured number of double coincidences corresponding to the LOR i and the β^+-γ-emitter is estimated by the equation:

$$\widetilde{b_i^{\gamma}} = \sum_k c_{i,k} \cdot \lambda_k^{\gamma} \tag{5}$$

where λ_k^γ is the image reconstructed in equation (2). From equations (3) to (5) we know that the number of detected double coincidences should be the sum of all $c_{i,k} \cdot \lambda_k^{\beta^+}$ plus the sum of all $c_{i,k} \cdot \lambda_k^\gamma$. Therefore, the reconstruction of the β^+-emitter image can be calculated as follows:

$$\begin{aligned} \lambda_{j,m+1}^{\beta^+} &= \frac{\lambda_{j,m}^{\beta^+}}{\sum_i \alpha_i c_{i,j}} \sum_i \frac{\alpha_i c_{i,j} b_i^D}{\alpha_i \left(\sum_k c_{i,k} \lambda_{k,m}^{\beta^+} + \sum_k c_{i,k} \lambda_{k,n}^{\gamma} \right)} \\ &= \frac{\lambda_{j,m}^{\beta^+}}{\sum_i \alpha_i c_{i,j}} \sum_i \frac{c_{i,j} b_i^D}{\sum_k c_{i,k} \lambda_{k,m}^{\beta^+} + \sum_k c_{i,k} \lambda_{k,n}^{\gamma}}. \end{aligned} \tag{6}$$

That is to say, in each iteration, the number of all detected double coincidences is compared with the sum of double coincidences (equations (4) and (5)). If both numbers are not in agreement, the reconstructed voxel value is changed accordingly. Again, the iteration is started with a homogeneous image with the same value for all voxels $\lambda_j^{\beta^+} = 1$.

Some pure β^+-emitter have more than one decay mode with corresponding branching ratios ε, e.g. for ^{18}F, decays with $\varepsilon_{\mathrm{EC}} = 3.14\%$ via electron capture without emission of annihilation photons and with $\varepsilon_{\beta^+} = 96.86\%$ via β^+ decay and subsequent emission of annihilating photons when surrounded by dense matter. Likewise, many β^+-γ-emitters can also decay without subsequent prompt-γ emission. These decays are indistinguishable from the decays of the pure β^+-emitter and must be correctly accounted for. While the ratio of the different decay branching ratios of the β^+-γ-emitter is inherently accounted for in the triple-to-double ratio, a branching ratio smaller than 1 for the pure β^+-emitter is not accounted for in equation (6). However, a correction for this branching ratio can be achieved with the usual cross-calibration of the β^+-emitter image values against a reference value. A similar cross-calibration can be conducted for equation (2) to allow for accurate quantification.

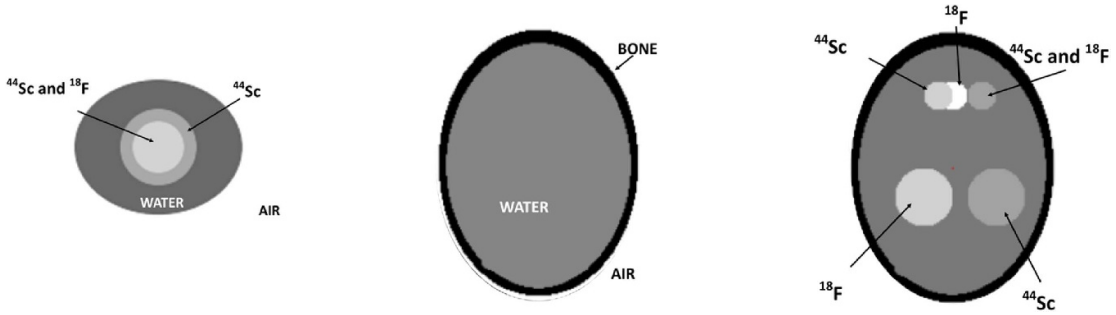

Figure 4. Left: illustration of cylinders simulated in scenario 1: the largest ellipsoidal cylinder is filled with water. The inner circular cylinder is filled with ^{18}F and ^{44}Sc. Middle: illustration of the fictive skull used in the simulations. The outer part (black) is bone, while the inner part (gray) is filled with water and tracer as described. The skull is surrounded by air. Right: second scenario: five cylinders: in the upper row, three partially over-lapping cylinders are simulated. The left cylinders is filled with ^{44}Sc, the middle cylinder is filled with ^{18}F, and the cylinder on the right is filled with both isotopes. In the lower row, is the left cylinder filled with ^{18}F and the right cylinder filled with ^{44}Sc.

2.6. Simulations

We tested our reconstruction approach on data simulated with the Geant4 simulation toolbox, version 11.1.1, on a Linux 5.15.0 system with Ubuntu 20.04.6. We simulated a fictional PET scanner with a diameter of 30 cm, 10 rings, and a 10 cm axial length. Each ring consisted of 36 detector blocks. Each detector block contained 440 (44 $\times$ 10) LSO crystals with a size of 2 $\times$ 2 $\times$ 20 mm. Detector resolution was not corrected for in the reconstruction, although some contributions as detector granularity and depth-of-interaction were included in the simulations. Intercrystal scatter events and optical crosstalk were not included in the analysis and will be addressed in a separate study. The crystal efficiency varies across photon energies and is included in the simulation.

We tested our reconstruction algorithm using the β^+-γ-emitter Scandium-44 (^{44}Sc), in combination with the β^+-emitter ^{18}F. Tracer characteristics are displayed in table 1.

In the first scenario, we simulated an ellipsoidal cylinder with axes measuring 8 cm and 6 cm, and a height of 4 cm height. This ellipsoidal cylinder was filled with water and positioned in the middle of the FOV. Inside this ellipsoidal cylinder, we placed a smaller cylinder with a radius of 3 cm and a height of 2 cm. This smaller cylinder consists of one inner cylinder with a radius of 2 cm and filled with 2.5 MBq of ^{18}F and with 1.75 MBq of ^{44}Sc and the outer part of the cylinder which was filled with 1.75 MBq ^{44}Sc. See figure 4 for an illustration. A scan duration of 120 s was simulated. ^{44}Sc has a longer decay time than ^{18}F. Therefore, one additional simulation of scenario 1 was obtained where the inner cylinder was filled with half of the activity (1.25 MBq) of ^{18}F. The amount of ^{44}Sc remained the same. The result of this experiment is displayed in the supplemental information, section 4.

In the second scenario, a skull-like structure was simulated. The skull consisted of two overlapping elliptic cylinders: the axes of the larger cylinder were 10.35 cm and 13.8 cm in length and contained bone tissue with a thickness between 1.414 cm and 1.69 cm in the trans-axial direction. The smaller cylinder had axes with lengths of 8.936 cm and 12.110 cm and was filled with water. Both simulated cylinders yielded an axial extension of 2 cm. For an illustration of the simulated objects, see figure 4. In total, five cylinders were simulated. Three of these cylinders, each with a radius of 1 cm, were filled with 1.25 MBq of the respective radiotracer: one contained only ^{18}F, one was filled with the ^{44}Sc, and one included both tracers. Two of these smaller cylinders overlapped as shown in figure 4. Two larger cylinders, each with a radius of 2 cm were also included: one was filled with 2.5 MBq of ^{18}F, and one was filled with 2.5 MBq of ^{44}Sc. The simulation for this setup also had a scan duration of 120 s.

From the simulated data, all coincidences consisting of two detected photons with an energy between 400 and 600 keV were considered double coincidences. For the tracer ^{44}Sc, a photon with an energy larger than 650 keV in combination with a double coincidence was considered a triple coincidence. All images were reconstructed to an image size of 128 $\times$ 128 $\times$ 50 with a voxel size of 2.5 $\times$ 2.5 $\times$ 2 mm without any smoothing. The normalization factors were calculated once for the specific scanner geometry and attenuation and were then included in the reconstruction procedure.

The reconstruction of the images was performed with Python 3.11.

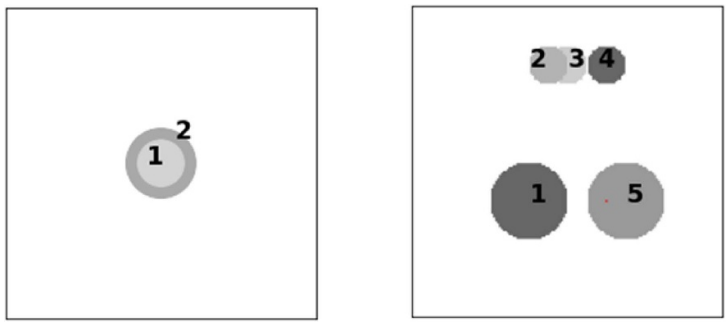

Figure 5. Image regions used to evaluate the reconstruction algorithm for scenario 1 (left) and scenario 2 (right).

2.7. Evaluation

2.7.1. Validation of estimated triple-to-double ratio

To assess the impact of attenuation, we compared the triple-to-double ratio with and without the inclusion of attenuation. Next, to illustrate systematical errors arising from a mismatch in object attenuation, we compared the estimated ratio acquired using the real object attenuation and a cylindrical phantom. The water-filled cylindrical phantom with a radius of 15 cm and a height of 4 cm was placed in the middle of the FOV. We compare both ratios and the images reconstructed using the ratio not belonging to the object. The visual results are displayed in the supplemental material, section 3.

Next, to validate the estimated triple-to-double ratio dependent on position in the FOV, branching ratios, and attenuation, we positioned a point source in different locations across the FOV diagonal in the scanner containing the simulated skull. We compared the calculated ratio and the ratio derived by the simulations.

2.7.2. Number of detected coincidences

Next, we compare the percentage of detected coincidences for both tracers. We are especially interested in the percentage of detected double and triple coincidences originating in the β^+-γ-emitter.

2.7.3. Evaluation of the reconstruction algorithm

To evaluate the proposed approach, we compared the reconstructed mean image intensities in specific volumes of interest (VOIs) with the mean expected image intensities. As our reconstructed images yield a high noise level, we include the intensity values between the first and the 99th percentile of a VOI to calculate the mean intensities of the VOIs. In the simulations, a tag indicating the corresponding isotope was added to the detected coincidence. To calculate the expected image intensities, the double coincidences belonging to the different nuclides were separated using the tag information from the simulations. Using the double coincidences corresponding to each isotope, the ground truth images (GT) are reconstructed using the conventional ML-EM algorithm. To visualize the images, 2 mm Gaussian smoothing was applied.

Hereby, we analyze the image regions as displayed in figure 5. We compare:

- regions where only the β^+-γ-emitter is present in the image: these include region 2 in scenario 1 and regions 2 and 5 in scenario 2: for these regions, we compared: (1) the percentage difference between the mean remaining intensity in the pure β^+-image and the mean expected intensity of the β^+-γ-emitter, (2) the mean expected β^+-γ intensity versus the reconstructed intensity
- for all other regions, we assessed the percentage difference between the mean intensity present in these regions of the β^+-emitter images reconstructed with our algorithm and the corresponding mean expected intensity.

2.7.4. Algorithm convergence

To analyze algorithm convergence, we compared the mean intensity in the defined VOIs across iterations in both the reconstructed images and the corresponding GT images. Additionally, the remaining intensity in the β^+-emitter image in regions where only the β^+-γ-emitter was present was calculated and compared across iterations.

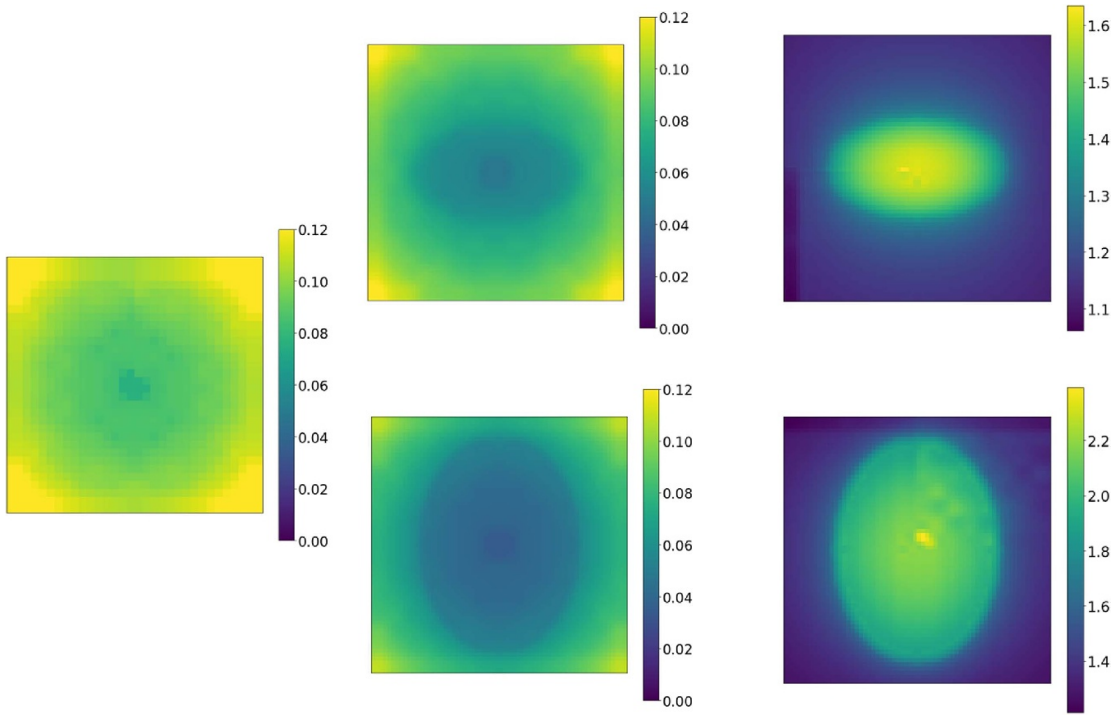

Figure 6. Triple-to-double ratio for the middle image slice of scenario 1 (upper row) and scenario 2 (lower row): Left: ratio dependent on the position in the FOV. As this ratio is scanner dependent, it is the same for scenarios 1 and 2. A value of e.g. 0.1 reflects that if one triple event is detected, it is expected that 10 double events with origin in the β^+-γ-emitter have been emitted. Middle: ratio dependent on position in FOV and corresponding attenuation. A value of 0.1 means that if one triple event is detected, 10 double events are expected. Right: ratio between triple-to-double ratio dependent on FOV position only and triple-to-double ratio dependent on attenuation and FOV position.

3. Results

3.1. Triple-to-double ratio

The triple-to-double ratio matrix before and after the inclusion of attenuation is displayed in figure 6 for scenario 2. As can be seen, the ratio is lowest in the center of the image and increases towards the image borders. In this context, a ratio of, 0.0714, for instance, corresponds to 14 ($\frac{1}{14} = 0.0714$) expected double coincidences when one triple coincidence is detected. Overall, the attenuation of the object multiplies the FOV-dependent triple-to-double ratio by factors between 0.62 and 0.90 for scenario 1 and between 0.45 and 0.71 for scenario 2.

Figure 7 shows the simulated and calculated triple-to-double ratios for the middle slice of the image. The absolute percentage difference between the simulations and calculations ranges from 4.5% to 6.6%.

In figure 8, the estimated triple-to-double ratio for the cylindrical phantom and the percentage difference between this ratio and the ratio obtained with our simulated objects is displayed. As illustrated, the cylindrical phantom overestimates the triple-to-double ratio when compared with scenario 1 by a factor of 5%–22%. For scenario 2, the absence of a matching attenuation map underestimates the triple-to-double ratio by 10%–45% depending on the position in the FOV. These differences have an impact on the reconstructed images as displayed in supplemental material, section 3.

3.2. Number of detected coincidences

The percentages of detected double and triple coincidences for both nuclides are displayed in table 2. As can be seen, in the first scenario, a larger percentage of simulated events is detected due to the lower attenuation of the object and the placement in the middle of the FOV. 4.7% and 4.0% of the detected coincidences of ^{44}Sc were triple coincidences, for scenario 1 and 2, respectively.

3.3. Reconstruction results

Results after 5, 10, and 20 iterations of the reconstruction algorithm for both scenarios and the tracer ^{44}Sc are displayed in figure 9. As can be seen, after the first iteration, the β^+-emitter image yields considerably smaller intensity values than the β^+-γ-emitter image. Additionally, the contribution of the β^+-γ-emitter is

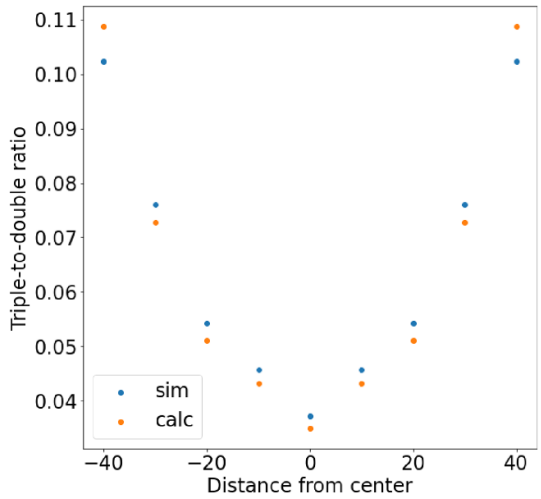

Figure 7. Comparison of MC simulated and calculated triple-to-double ratio with prompt γ attenuation for the ^{44}Sc based tracer. Relative statistical uncertainties of the simulated ratios are for all cases <0.05.

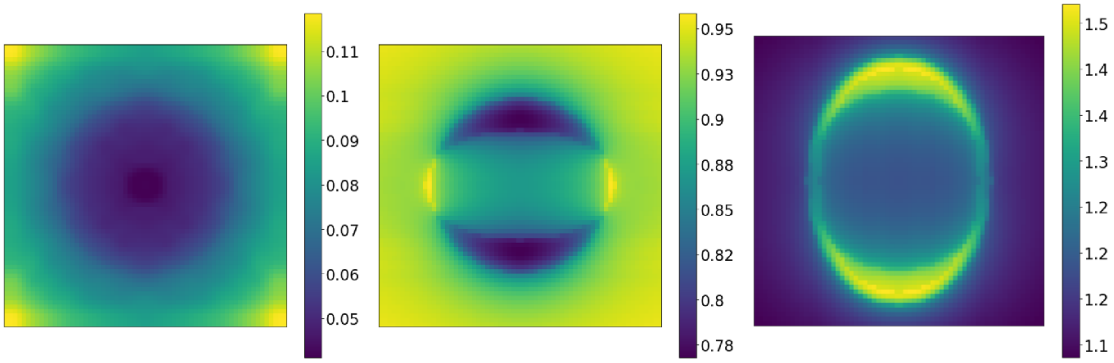

Figure 8. Triple-to-double ratio using a surrogate attenuation map of a cylindrical phantom instead of the attenuation map of the imaged object. The figure shows the ratio of the middle image slice: Left: triple-to-double ratio dependent on the position in the FOV and attenuation of the cylindrical phantom. Middle: percentage of cylindrical triple-to-double ratio and the ratio of the object in scenario 1; Right: percentage of the triple-to-double ratio of cylindrical object and the skull simulated in scenario 2.

Table 2. Percentages of detected events for the different scenarios and nuclides.

Scenario	% total detected events	% detected triples ^{44}Sc	% detected doubles ^{44}Sc	% detected doubles ^{18}F
1	0.9 %	0.02 %	0.51 %	0.43 %
2	0.5 %	0.01 %	0.26 %	0.24 %

clearly visible. With increasing number of iterations, the contribution of the β^+-γ-emitter decreases and the intensity values of the β^+-emitter image increase.

In figure 10 the intensity values between GT and images reconstructed with our dual tracer approach (DT) of both scenarios are compared. As can be seen, in the first iterations, the β^+-emitter is highly underestimated when compared with the GT image. However, at iteration 20, the mean intensity values of the reconstructed image are in good agreement with the GT image for both scenarios. The mean intensity values of the β^+-γ-emitter are already at iteration 10 in good agreement with the GT. For scenario 1, the percentage difference between the mean intensity values in VOI 2 is 3.01% for the β^+-emitter image. For the β^+-γ-emitter image, the percentage difference between the mean values of GT and DT image is 10.3% for VOI 1 and VOI2. For scenario 2 and the β^+-emitter image, the absolute percentage differences between mean values of GT and reconstructed images result in 4.2% for the largest VOI (VOI 1), 6.6% for VOI 3, and 7.4% for VOI 4, respectively. For the same scenario and β^+-γ-emitter image, the absolute percentage differences between GT and reconstructed image are 8.7% for VOI 2, 9.4% for VOI 4, and 10.8% for VOI 5. Results of the reconstructions using the attenuation map corresponding to the cylindrical object are displayed in the supplemental material. For scenario 1, the intensity values of the β^+-emitter image were

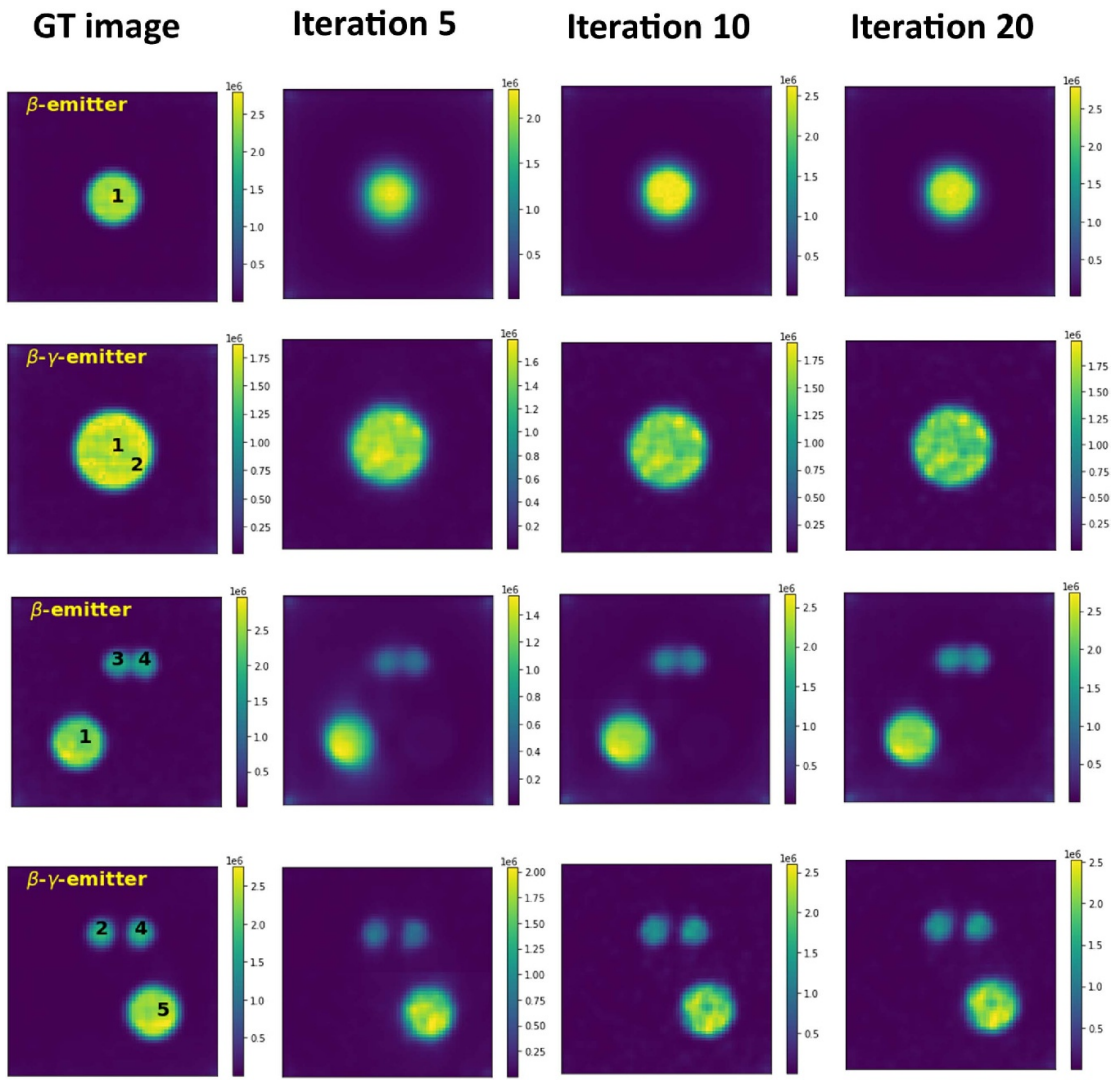

Figure 9. Reconstructed images for scenario 1 (two upper rows) and scenario 2 (two lower rows). First and third row: pure β^+-emitter images, second and forth row: β^+-γ-emitter images. From left to right: ground truth image reconstructed with the double coincidences corresponding to the respective isotope. The VOI numbers are placed in the corresponding regions for a better overview. Reconstructed images after 5, 10, and 20 iterations. In the fifth iteration, the β^+-emitter image yields lower intensity values than the β^+-γ-emitter image, especially in the overlapping image regions. With increasing iterations, the intensity values become comparable. In scenario 2, it can be seen that the cylinder containing both tracers, yields lower intensity values than the other cylinders. However, with increasing iterations, the intensity values become comparable. Please note the different intensity scales across the number of iterations.

underestimated by 28.8% while the intensity values of the β^+-γ-emitter image were overestimated by 35%. For scenario 2, the intensity values in the β^+-emitter image were overestimated by 12% (VOI 1), 16% (VOI 3), and 21% (VOI 4). In the β^+-γ-emitter image, the intensity values were underestimated by 26% (VOI 2), 28% (VOI 4), and 27% (VOI 5).

3.4. Algorithm convergence

Figure 11 shows that the algorithm converges for both reconstructed images. The mean intensity present in the regions of interest becomes stable after a few iterations. The β^+-emitter image reaches low intensity values in the first iterations when compared with the corresponding GT image. However, after several more iterations, the intensity values between the GT image and the reconstructed image match. In general, the remaining intensity values in the regions of the β^+-emitter image where only the β^+-γ-emitter was simulated decreased with an increasing number of iterations. For both scenarios (figure 11, right), the mean intensity values approach a stable value of spurious residual activity of 3.7% for VOI 2 in scenario 1, 3.8% for VOI 3 and 0.2% for VOI 5 in scenario 2. In conclusion, a small bias of the β^+-γ-emitter remains in the β^+-emitter image.

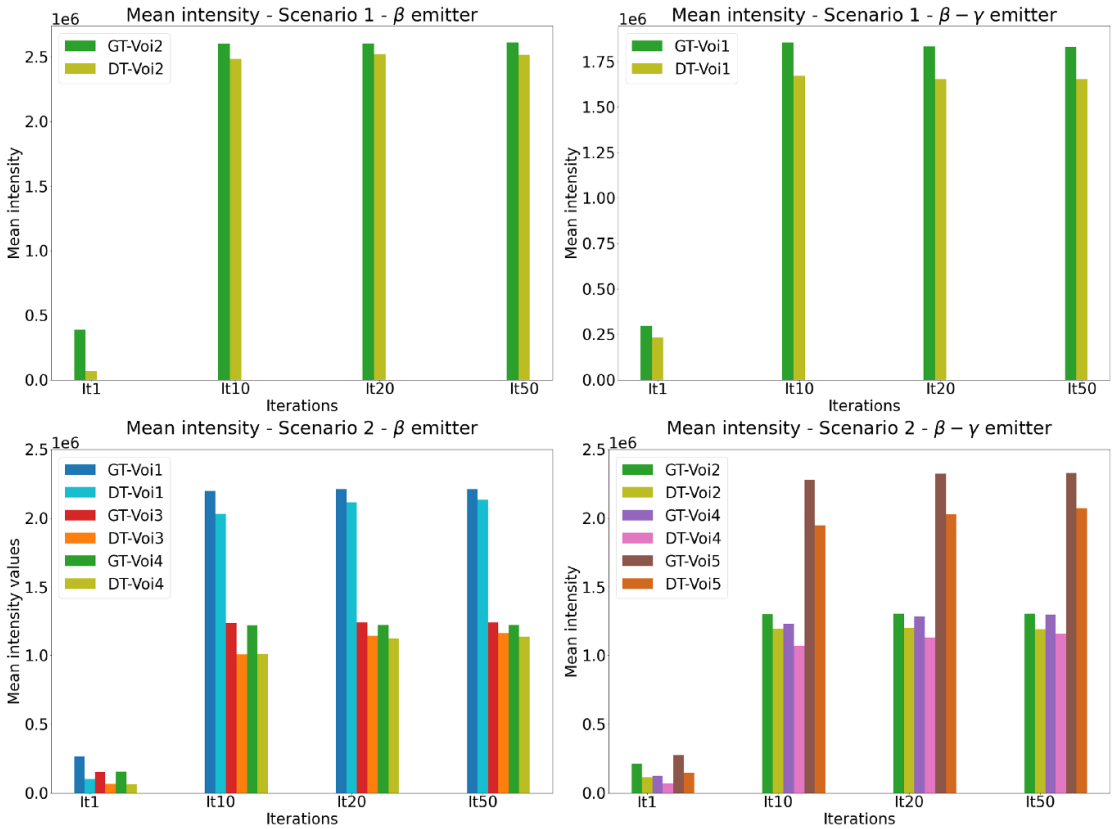

Figure 10. Comparison of the mean intensity values after eliminating outlier voxels of the ground truth image (GT) and the image reconstructed with the dual-tracer reconstruction method (DT) for iterations 1, 10, 20, and 50. Upper row: scenario 1, lower row: scenario 2; Left: pure β^+-emitter image; Right: β^+-γ-emitter image.

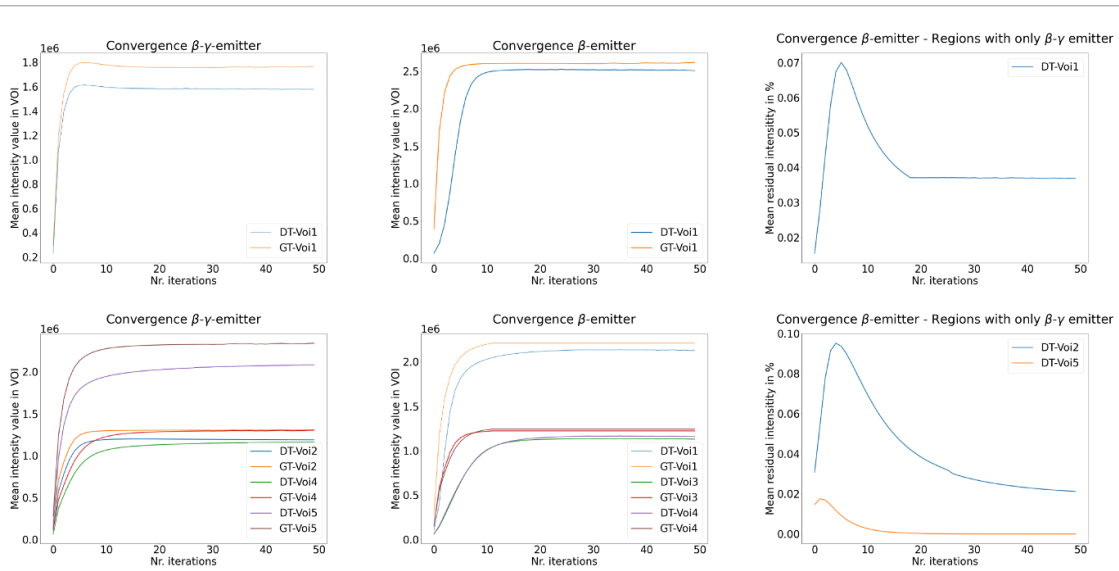

Figure 11. Convergence of the reconstruction algorithm: Upper row: scenario 1, lower row: scenario 2. Left: mean intensity value in VOIs containing β^+-γ-emitter. Middle: mean intensity value in VOIs containing β^+-emitter. Please note that VOI 3 and 4 also contain the β^+-γ-emitter. As seen in the curve, in this cases, the intensity is underestimated in the first iterations but recovers subsequently and converges towards the ground truth. Right: percentage difference of regions in β^+-emitter image containing only the β^+-γ-emitter. As can be seen, in the first iterations a considerably large amount of the β^+-γ-emitter is still present. However, this amount decreases with increasing iterations.

4. Discussion

This work aimed to demonstrate the feasibility of the ML-EM algorithm for the reconstruction of dual tracer PET images including attenuation. To use the developed reconstruction method for imaging of real objects with real scanners, random and scatter correction methods need to be adapted and integrated into the algorithm. The advantage of our algorithm is that it allows the incorporation of random and scatter correction in the way as it is done in conventional the ML-EM based reconstruction algorithm, i.e. as precorrection or by incorporation into the forward model. Random correction methods for triple coincidences have been proposed by Niekämper *et al* (2023). Fast MC simulations for scatter estimation in PET has been realized recently by Scheins *et al* (2021). Using a full MC approach, the adaptation of the method for estimation of scatter contributions for the prompt γ of the β^+-γ-emitter is straight forward. The estimated scatter for both emitters can then be included in the ML-EM algorithm as it is conventionally done.

The feasibility of our approach has been demonstrated using simulations of tracers based on ^{18}F and ^{44}Sc. However, our approach can be used to separate any pure β^+-emitter and a β^+-γ-emitter emitting a high-energy prompt γ-photon, with arbitrary branching ratio of the isotopes. Equations (2) and (6) are still valid in the case that no pure β^+-emitter is present. In this case, the double image represents a reconstructed image that appropriately handles the low fractions of prompt γ-photons which lead to spurious double coincidences in the conventional ML-based reconstruction and therefore to a quantization error. Therefore, the presented approach can be used to reconstruct PET images acquired with only one β^+-γ-emitter, emitting a high-energy γ-photon such as ^{68}Ge, which may lead to improved quantification accuracy.

In contrast to other works, we included object attenuation in the reconstruction process. Previous works either assumed a constant triple detection efficiency across the FOV (Sitek *et al* 2011) or estimated the joint influence of attenuation and detection efficiency by scanning of a cylindrical phantom (Pratt *et al* 2023). Using a scan of a cylindrical phantom has the advantage that it intrinsically accounts for scatter contribution. However, it is only a very approximate indication of the object dependency of the attenuation. While this approach works well for small objects like rodents, we showed that the use of a phantom scan leads to substantial quantitative errors in the reconstructed images for larger objects as used in our simulated scenarios. In addition, the scatter correction of a phantom scan will likely lead to quantitation errors due to the mismatch of both phantoms.

Other groups have used CNNs to separate the images of two radiotracers (Zeng *et al* 2023, Fang *et al* 2024). While these works have demonstrated good results on simulated brain data, the networks cannot be used for other body parts (Fang *et al* 2024) without retraining. A clear advantage of our proposed method is that it does not require training data providing a general approach for dual tracer PET imaging of any body part. However, the images reconstructed with CNNs resulted in images with less noise. Therefore, we will consider the use of neural networks for image denoising in future work. In the present work, we estimated the triple-to-double ratio by calculating the γ-photon attenuation for each path between each voxel and each detector element using ray tracing with a single ray for each detector element. This can only provide an approximation of the corresponding attenuation factor and more precise estimation techniques such as tubes of response (Scheins *et al* 2006) might give a more exact estimation.

Alternatively, a neural network can be trained to estimate this ratio. A large number of different attenuation maps and the FOV-dependent ratio can be used as network input and the corresponding triple-to-double ratios including attenuation acquired by simulations can serve as the GT. This approach might also lead to more accurate results. We will explore this opportunity in future work.

In our work, we separated double and triple coincidences by using information of the MC simulations. In a real world scenario, the separation of double and triple events will likely not be that accurate. However, as previous groups demonstrated that both coincidence groups can be separated by using scanner information (Andreyev *et al* 2014, Pratt *et al* 2023), we assume that this will have little impact on our reconstruction results.

Our algorithm still leads to quantification errors. These errors could be due to an over-estimation of the β^+-γ-emitter image. A more precise estimation of the triple-to-double ratio would potentially help to decrease this error and result in better quantitative results. Additionally, the correct inclusion of scatter and random correction is also expected to improve the quantification accuracy. We will consider all these aspects in future work.

The reconstructed β^+-γ-emitter image shows a high level of noise. This noise is mainly due to the limited detection efficiency of the triple coincidences in our simulations due to the limited efficiency of our fictional scanner (approx. 1.4%). However, our results show that our algorithm was accurate despite the limited detection efficiency in our simulations. Consequently, increased detection efficiency can be expected to reduce the noise level. In other works, the image is smoothed after every iteration to suppress noise (Pratt *et al* 2023). An alternative method for noise reduction is the use of use priors during image reconstruction,

which can be implemented our reconstruction approach (Schramm and Holler 2022). In this respect, one possibility in addition of the root mean prior, would be to use the image reconstructed with all double coincidences of the β^+-γ-emitter as prior for our proposed reconstruction procedure. Finally, a higher detection efficiency is typically found in the latest generation of developed PET scanners, e.g. the in-house developed 7T MR compatible BrainPET insert, (Lerche *et al* 2023). Measurements with this scanner are expected to confirm our simulation results.

The presented algorithm is designed to work with β^+-γ-emitters emitting a high-energy γ-photon. In future work, we will extend our approach to nuclides emitting γ-photons with an energy close to the 511 keV energy of the β^+-coincidence photons such as Iodine-124 (^{124}I) or Yttrium-89 (^{89}Y). Additionally, we will also extend our algorithm for β^+-γ-emitters emitting cascades of several prominent γ-photons. In the case of cascade γ-photons, machine learning algorithm could be included to distinguish double coincidences of the two annihilation photons and double coincidences of e.g. two (down-scattered) prompt γ-photons.

5. Conclusion

In this work, we have presented an ML-EM-based algorithm to reconstruct dual tracer PET images simultaneously and quantitatively. We focused on separating images of one pure β^+-emitter and one β^+-γ-emitter emitting a high energy prompt γ-photon. The prompt γ-photon is used to identify the tracer to which the events belong. We estimated the number of double coincidences originating from the β^+-γ-emitter using a triple-to-double ratio based on the position of the source in the FOV accounting for the object-dependent attenuation of the prompt γ-photon. By incorporating this estimation in the forward projection of the ML-EM algorithm, we ensure that proper incorporation of scatter and random correction can easily be implemented at a later stage. The results on simulated images are very promising: In the β^+-emitter images, only a small bias between 0.4% and 3.8% of the β^+-γ-emitter remained. For both images, our algorithm still leads to quantification errors in both reconstructed images ranging from 3% to 10%. We demonstrated that a mismatch in the real attenuation β^+-γ-emissions of the object and the attenuation implemented in the reconstruction leads to quantification errors, and that appropriate attenuation correction improves the accuracy. With a more exact estimation of the triple-to-double ratio and the inclusion of a proper scatter correction, these quantification errors potentially can be further decreased. Our approach can and will be extended to other isotopes emitting γ-photons in the same energy window as the two annihilation photons or emitting cascade γ photons. This will allow the reconstruction of dual tracer PET images with high quantitative accuracy in the future.

Data availability statement

The data that support the findings of this study are available upon reasonable request from the authors. https://doi.org/10.5281/zenodo.13382959.

Acknowledgments

Funded by the European Union

This work is funded by the European Union, Marie-Curie Sklodowska Fellowship HORIZON-MSCA-2021-PF-01, Grant 101068572.

ORCID iDs

Elisabeth Pfaehler https://orcid.org/0000-0002-6160-3011
Jürgen Scheins https://orcid.org/0000-0003-3474-430X
N Jon Shah https://orcid.org/0000-0002-8151-6169
Christoph W Lerche https://orcid.org/0000-0003-2749-2108

References

Andreyev A and Celler A 2011 Dual-isotope PET using positron-gamma emitters *Phys. Med. Biol.* **56** 4539
Andreyev A, Sitek A and Celler A 2014 Em reconstruction of dual isotope PET using staggered injections and prompt gamma positron emitters *Med. Phys.* **41** 022501
Black N F, McJames S and Kadrmas D J 2009 Rapid multi-tracer PET tumor imaging with F-FDG and secondary shorter-lived tracers *IEEE Trans. Nucl. Sci.* **56** 2750–8

Chételat G et al 2020 Amyloid-PET and 18F-FDG-PET in the diagnostic investigation of Alzheimer's disease and other dementias *Lancet Neurol.* **19** 951–62
Conti M and Eriksson L 2016 Physics of pure and non-pure positron emitters for PET: a review and a discussion *EJNMMI Phys.* **3** 1–17
Dehdashti F, Mintun M, Lewis J, Bradley J, Govindan R, Laforest R, Welch M and Siegel B 2003 *In vivo* assessment of tumor hypoxia in lung cancer with 60 Cu-ATSM *Eur. J. Nucl. Med. Mol. Imaging* **30** 844–50
Erba P, Sollini M, Lazzeri E and Mariani G 2013 FDG-PET in cardiac infections *Seminars in Nuclear Medicine* vol 43 (Elsevier) pp 377–95
Fang J, Zeng F and Liu H 2024 Signal separation of simultaneous dual-tracer PET imaging based on global spatial information and channel attention *EJNMMI Phys.* **11** 47
Fukuchi T, Shigeta M, Haba H, Mori D, Yokokita T, Komori Y, Yamamoto S and Watanabe Y 2021 Image reconstruction method for dual-isotope positron emission tomography *J. Instrum.* **16** 01035
Gao F, Liu H, Jian Y and Shi P 2009 Dynamic dual-tracer PET reconstruction *Information Processing in Medical Imaging: 21st Int. Conf., IPMI 2009 (Williamsburg, VA, USA, 5–10 July 2009). Proc. 21* (Springer) pp 38–49
Graves S *et al* 2015 Novel preparation methods of 52Mn for immunoPET imaging *Bioconjug. Chem.* **26** 2118–24
Hernandez R, Valdovinos H, Yang Y, Chakravarty R, Hong H, Barnhart T and Cai W 2014 ^{44}Sc: an attractive isotope for peptide-based PET imaging *Mol. Pharm.* **11** 2954–61
Kadrmas D, Rust T and Hoffman J 2013 Single-scan dual-tracer FLT+FDG PET tumor characterization *Phys. Med. Biol.* **58** 429
Lerche C *et al* 2023 First performance results of a UHF-MRI compatible BrainPET insert for neuroscience *2023 IEEE Nuclear Science Symp., Medical Imaging Conf. and Int. Symp. on Room-Temperature Semiconductor Detectors (NSS MIC RTSD)* (IEEE) pp 1–2
Meikle S *et al* 2021 Quantitative PET in the 2020s: a roadmap *Phys. Med. Biol.* **66** 06–01
Michel C, Sibomana M, Boi A, Bernard X, Lonneux M, Defrise M, Comtat C, Kinahan P and Townsend D 1998 Preserving Poisson characteristics of PET data with weighted OSEM reconstruction *1998 IEEE Nuclear Science Symp. Conf. Record. 1998 IEEE Nuclear Science Symp. and Medical Imaging Conf. (Cat. No. 98CH36255)* vol 2 (IEEE) pp 1323–9
Myers W G 1973 Radiopotassium-38 for *in vivo* studies of dynamic processes *J. Nucl. Med.* **14** 359–60
Niekämper D, Scheins J, Shah N, Lopez-Herraiz J and Lerche C 2023 Precise and accurate coincidence processing for the BrainPET-7T with triple coincidences and randoms *2023 IEEE Nuclear Science Symp., Medical Imaging Conf. and Int. Symp. on Room-Temperature Semiconductor Detectors (NSS MIC RTSD)* (IEEE) p 1
Pratt E *et al* 2023 Simultaneous quantitative imaging of two PET radiotracers via the detection of positron–electron annihilation and prompt gamma emissions *Nat. Biomed. Eng.* **7** 1028–39
Rust T, DiBella E, McGann C, Christian P, Hoffman J and Kadrmas D 2006 Rapid dual-injection single-scan 13N-ammonia PET for quantification of rest and stress myocardial blood flows *Phys. Med. Biol.* **51** 5347
Salaün P *et al* 2020 Good clinical practice recommendations for the use of PET/CT in oncology *Eur. J. Nucl. Med. Mol. Imaging* **47** 28–50
Scheins J, Boschen F and Herzog H 2006 Analytical calculation of volumes-of-intersection for iterative, fully 3-D PET reconstruction *IEEE Trans. Med. Imaging* **25** 1363–9
Scheins J, Lenz M, Pietrzyk U, Shah N and Lerche C 2021 High-throughput, accurate Monte Carlo simulation on CPU hardware for PET applications *Phys. Med. Biol.* **66** 185001
Schramm G and Holler M 2022 Fast and memory-efficient reconstruction of sparse Poisson data in listmode with non-smooth priors with application to time-of-flight PET *Phys. Med. Biol.* **67** 155020
Sitek A, Andreyev A and Celler A 2011 Reconstruction of dual isotope PET using expectation maximization (EM) algorithm *2011 IEEE Nuclear Science Symp. Conf. Record* (IEEE) pp 4323–6
Steinberger W *et al* 2024 Positronium lifetime validation measurements using a long-axial field-of-view positron emission tomography scanner *EJNMMI Phys.* **11** 76
Topping G, Schaffer P, Hoehr C, Ruth T and Sossi V 2013 Manganese-52 positron emission tomography tracer characterization and initial results in phantoms and *in vivo Med. Phys* **40** 042502
Umbricht C, Benešová M, Schmid R, Türler A, Schibli R, Meulen N and Müller C 2017 ^{44}Sc-PSMA-617 for radiotheragnostics in tandem with ^{177}Lu-PSMA-617-preclinical investigations in comparison with ^{68}Ga-PSMA-11 and ^{68}Ga-PSMA-617 *EJNMMI Res.* **7** 1–10
Zeng F, Fang J, Muhashi A and Liu H 2023 Direct reconstruction for simultaneous dual-tracer PET imaging based on multi-task learning *EJNMMI Res.* **13** 7